FACULTY OF NUCLEAR SCIENCES AND PHYSICAL ENGINEERING CTU IN PRAGUE

GHENT UNIVERSITY

Unfolding Runaway Electron Parameters from Bremsstrahlung Radiation in Tokamaks

Doctoral programme:	Physics of plasma and thermonuclear fusion
Applicant:	Ing. Marek Tunkl
Supervisors CTU:	Ing. Vojtěch Svoboda, CSc.
Supervisors UGhent:	Prof. Dr. Roger J. E. Jaspers
Year:	2026

Abstract

Runaway electrons (REs) represent challenges for tokamak fusion devices, as high-energy electron beams generated during plasma disruptions can cause damage to plasma-facing components (PFCs). Reliable diagnostics capable of reconstructing runaway electron parameters are therefore essential for present experiments, so that robust mitigation strategies can be developed. This work investigates methods for inferring runaway electron properties from bremsstrahlung hard X-ray (HXR) radiation measurements and extends existing approaches beyond energy reconstruction to additional parameters of interest.

A forward model was developed for the GOLEM tokamak that combines Monte Carlo simulations of bremsstrahlung production, photon transport, and detector response.

The results demonstrate that the anisotropic nature of bremsstrahlung emission provides useful information for estimating runaway electron strike-point locations and indicates the potential for pitch-angle inference. The study highlights both the capabilities and limitations of bremsstrahlung-based diagnostics and provides a path for further development of runaway electron parameter reconstruction methods.

Contents

1. Motivation

Thermonuclear fusion represents a long-term solution to the global demand for energy, offering the potential for large-scale power generation with minimal greenhouse gas emissions. Among the various confinement concepts, magnetic confinement fusion in the tokamak configuration has reached the highest level of technological maturity. The ITER experiment represents the next major step toward reactor-relevant plasma conditions and will operate with unprecedented plasma current, stored magnetic energy, and pulse duration.

Despite this progress, several physics challenges must be resolved before fusion can become a reliable energy source. One of the most critical issues for reactor-scale tokamaks is the generation and confinement of runaway electrons.

The danger associated with runaway electrons is their potential to form localized, high-energy beams during disruption events. When such beams are lost and impact plasma facing components, their kinetic energy can be deposited over small areas, leading to mechanical damage [1].

Measurements of runaway electrons rely primarily on secondary radiation. Commonly employed diagnostics include synchrotron radiation imaging, electron cyclotron emission, and bremsstrahlung hard X-ray (HXR) measurements. Bremsstrahlung radiation is emitted when runaway electrons interact with plasma ions or with high-Z plasma-facing materials. The measured HXR spectra encodes information about the runaway electron energy distribution, pitch angle. However, extracting quantitative runaway parameters from measured spectra is a non-trivial inverse problem requiring forward modeling.

Small and medium-sized tokamaks can provide a platform for development and validation of runaway diagnostics under fusion-relevant conditions. The GOLEM tokamak offers an environment for systematic studies of runaway generation and plasma facing component (PFC) interaction. Although GOLEM operates at modest parameters. The approaches for bremsstrahlung emission and detector response modeling are scale-independent.

The aim of this work is to extend existing methods for reconstructing runaway electron parameters from bremsstrahlung HXR measurements. Combining detailed Monte Carlo modeling HXR generation and transport, detector response simulations and regularized inversion techniques tailored to spectral data provided from multiple sources.

2. Theory

This chapter summarizes the theory of runaway electrons. First, the basic physics of runaway electron generation in tokamak plasmas is introduced. Briefly, the radiation mechanisms relevant for runaway diagnostics are discussed. Finally, the mathematical methods for solving inverse problems and regularization techniques used for parameter reconstruction are presented.

2.1. Runaway Electron Physics

In a tokamak plasma, electrons are subject to acceleration by an induced toroidal electric field E_t. Under typical conditions, this acceleration is counteracted by momentum loss due to Coulomb collisions with the background plasma. For electron velocities up to the thermal velocity

$$v_\mathrm{th} = \sqrt{\frac{2k_\mathrm{B}T_\mathrm{e}}{m_\mathrm{e}}}, \tag{1}$$

the collisional friction force increases.

However, at supra-thermal velocities the collisional drag decreases approximately as v^{-2}. Therefore, a critical velocity v_c exists above which electrons experience net acceleration and may continuously gain energy – they *run away*.

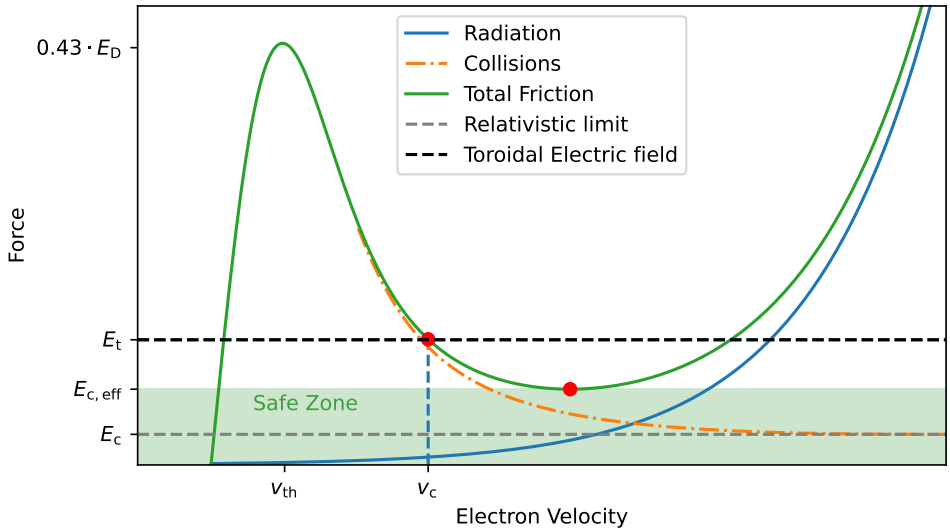

Figure 1: Overview of forces acting on electron.

Relativistic treatment of collisional drag gives an equivalent electric field E_c which can represent a simple threshold for runaway electron (RE) generation:

$$E_c = \frac{n_\mathrm{e} e^3 \ln\Lambda}{4\pi\varepsilon_0^2 m_\mathrm{e} c^2}, \tag{2}$$

where e is elementary charge, ε_0 vacuum permittivity, m_e electron mass and c speed of light. This threshold field value depends primarily on the electron density n_e since the Coulomb logarithm $\ln\Lambda$ can be considered constant for tokamak plasmas.

At relativistic velocities, additional contributions to the force balance become important. In particular, radiation forces associated with synchrotron and bremsstrahlung radiation limits maximum reachable energy. The combined effect of collisional drag and radiation losses results in a local minimum within the runaway region represented by effective critical electric field $E_{\mathrm{c,eff}}$. Experimentally, it was determined that the threshold for RE generation $E_{\mathrm{c,eff}}$ is 3–5 times larger than E_{c} [2].

A second important scale is the Dreicer field

$$E_{\mathrm{D}} = \frac{n_{\mathrm{e}} e^3 \ln \Lambda}{4\pi\varepsilon_0^2 k_{\mathrm{B}} T_{\mathrm{e}}}, \tag{3}$$

which characterizes the electric field required for electrons at the thermal velocity to overcome collisional drag over one mean free path [3]. In most tokamak scenarios the electric field satisfies

$$E_{\mathrm{t}} < E_{\mathrm{c,eff}} \ll E_{\mathrm{D}}, \tag{4}$$

so REs are generated only in transient events, like plasma startup phase and disruptions. The overview of the discussed forces can be found on figure Figure 1.

2.2. Runaway generation mechanisms

There are two main REs generation mechanisms, the *Dreicer mechanism* and the *avalanche mechanism*. In the Dreicer generation, electrons from the thermal population gradually runaway due to continuous acceleration by the electric field. In contrast, the avalanche mechanism relies on the presence of an existing runaway population, which is multiplied through collisions with bulk electrons, resulting in exponential growth [4].

The Dreicer mechanism is a primary source of runaway electrons, as it does not require a pre-existing runaway population. Another primary mechanism, referred to as the *hot-tail* mechanism, arises during rapid changes in plasma conditions, most notably during fast cooling events. For long-duration discharges, all potential sources of runaway electrons must be considered, since even an initially negligible runaway population can be strongly amplified through avalanche multiplication.

The relative importance of these mechanisms depends strongly on plasma parameters such as density, temperature, current, and device size.

For the GOLEM tokamak, Dreicer generation is the dominant, others are negligible due to the modest plasma parameters and short discharge duration.

2.2.1. Dreicer generation

The Dreicer mechanism describes the diffusive transition of electrons from the high-energy tail of a Maxwellian distribution into the runaway region under a constant electric field.

In Dreier's original formulation [5, 6], the plasma is assumed to be infinite, homogeneous, and non-relativistic, with an electron distribution function close to a Maxwellian and subject to a constant electric field. The interaction between an individual electron and the background plasma exhibits two distinct regimes, separated critical velocity v_{c}.

Electrons with velocity exceeding the critical value v_c experience net acceleration and gradually enter the runaway region. Since the background distribution function is continuously recovered by collisions, the Dreicer mechanism results in a continuous growth of runaway electrons.

An approximate expression for the rate of electron flux into the runaway region was derived by Connor and Hastie [7] and can be written as

$$\frac{\mathrm{d}n_{\mathrm{RE_D}}}{\mathrm{d}t} = Cn_{\mathrm{e}}\nu_{\mathrm{th}}\left(\frac{E}{E_{\mathrm{D}}}\right)^{-3\frac{1+Z_{\mathrm{eff}}}{16}} \exp\left(-\frac{1}{4\left(\frac{E}{E_{\mathrm{D}}}\right)} - \sqrt{\frac{1+Z_{\mathrm{eff}}}{\frac{E}{E_{\mathrm{D}}}}}\right), \tag{5}$$

where n_{e} is the electron density, ν_{th} is the thermal collision frequency

$$\nu_{\mathrm{th}} = \frac{n_{\mathrm{e}}e^4 \ln\Lambda}{4\pi\varepsilon_0^2 m_{\mathrm{e}} v_{\mathrm{th}}^3}, \tag{6}$$

Z_{eff} is the effective ion charge, and C is a numerical constant not determined by the theory.

2.2.2. Avalanche

Avalanche multiplication occurs when an existing runaway electron transfers sufficient energy to a thermal electron through collisions, therefore creating new runaway electrons. This process leads to exponential growth of the runaway population [4, 8].

Avalanche is negligible in small devices such as GOLEM. However, in large tokamaks, such as ITER, avalanche multiplication can convert a significant fraction of the plasma current into runaway current during disruptions. This represents one of the most serious risks for plasma-facing component damage in reactor-scale machines.

2.2.3. Radiation losses and diagnostics of runaway electrons

REs can lose energy through both radiative losses and particle losses, upon de-confinement and wall impact. The radiation is also a primary channel for RE diagnostics [4].

2.2.4. Electron cyclotron emission

Electron Cyclotron Emission (ECE) is produced by electrons undergoing gyro-motion around magnetic field lines. In non-relativistic conditions, electrons emit radiation at the cyclotron frequency and its harmonics, determined by the magnetic field strength. In thermal fusion plasmas, emission and absorption of ECE are in equilibrium, allowing ECE diagnostics to be used to measure the local electron temperature assuming black body radiation model.

When relativistic REs are present, a relativistic shift of the emission frequency breaks the equilibrium between emission and absorption. As a result, ECE can no longer reliably measure plasma temperature but can instead be used to detect the presence of REs with energies up to hundreds of keV.

2.2.5. Synchrotron radiation

At relativistic energies, radiation emitted by electrons gyrating in a magnetic field is commonly referred to as synchrotron radiation. In this regime the power is emitted at high

harmonics and forms a broad, nearly continuous spectrum. Synchrotron radiation is strongly anisotropic and depends sensitively on RE energy and pitch angle

In tokamak plasmas, synchrotron radiation from REs typically peaks in the near-infrared to mid-infrared wavelength range, although emission can extend into the visible spectrum depending on plasma parameters and device size. Imaging diagnostics in the visible or infrared range are therefore commonly used to observe synchrotron emission and infer properties such as beam location and qualitative features of the runaway electron distribution.

2.2.6. Bremsstrahlung

Bremsstrahlung ("braking radiation") is emitted when REs are deflected in Coulomb fields of ions or nuclei in plasma or in plasma-facing materials.

Bremsstrahlung emission forms a continuum with photon energies $E_{\mathrm{ph}} \leq E_{\mathrm{RE}}$. The angular distribution is strongly forward-peaked, with a characteristic opening angle of order $\sim \gamma^{-1}$, where γ is the Lorentz factor [9]. Therefore, the measured signal depends strongly on viewing geometry and line-of-sight alignment with the RE velocity.

2.3. Inversion and Regularization Methods

Inverse problems arise in many areas of experimental physics, where one seeks to infer an unknown quantity from indirect and noisy measurements. If we assume the forward model in the form

$$\boldsymbol{f} = \mathbf{T}\boldsymbol{x} + \boldsymbol{n}, \tag{7}$$

where $\boldsymbol{f}$ is the measured data vector, $\boldsymbol{x}$ the vector of unknown parameter, $\mathbf{T}$ the transfer (or response) matrix, and $\boldsymbol{n}$ measurement noise.

The objective of inversion is to estimate $\boldsymbol{x}$ given $\boldsymbol{f}$ and $\mathbf{T}$. In practice, this problem is often ill-posed: the matrix $\mathbf{T}$ may be ill-conditioned and small perturbations in the data can lead to unstable solutions. Regularization is therefore required to obtain physically meaningful reconstructions.

2.3.1. Tikhonov regularization

Tikhonov regularization stabilizes the inversion by introducing an additional constraint on the solution. The regularized solution is defined as the minimizer of the functional

$$\boldsymbol{x} = \arg\min(\|\mathbf{T}\boldsymbol{x} - \boldsymbol{f}\|^2 + \alpha\|\mathbf{L}\boldsymbol{x}\|^2), \tag{8}$$

where $\mathbf{L}$ regularization matrix and hyperparameter $\alpha \geq 0$ controls the strength of regularization imposed on solution.

There are commonly used regularizations $\mathbf{L}$:

- Zeroth-order regularization: With $\mathbf{L} = \mathbf{I}$ identity matrix which penalizes large values in solution $\boldsymbol{x}$
- First-order regularization: Matrix $\mathbf{L}$ of first order differences penalizes steep gradients in solution. In 2D space it has a form of $\mathbf{L} = \boldsymbol{\nabla}_x^T\boldsymbol{\nabla}_x + \boldsymbol{\nabla}_y^T\boldsymbol{\nabla}_y$, where $\boldsymbol{\nabla}_x$ and $\boldsymbol{\nabla}_y$ denote

finite-difference operators in the respective directions. Scaling factors can be introduced to impose anisotropic regularization.

2.3.2. Minimum Fisher Regularization (MFR)

Minimum Fisher Information Regularization (MFR) can be interpreted as an adaptive Tikhonov scheme. The regularization weights depend on the current estimate of $\boldsymbol{x}$, penalizing gradients more strongly in regions of small amplitude [10]. The method is implemented iteratively,

$$\mathbf{L} = \boldsymbol{\nabla}_x^T \mathbf{M}^{(n)} \boldsymbol{\nabla}_x + \boldsymbol{\nabla}_y^T \mathbf{M}^{(n)} \boldsymbol{\nabla}_y \tag{9}$$

where $\mathbf{M}^{(n)}$ is a diagonal weight matrix updated at each iteration.

$$\begin{aligned} M_{ij}^{(n)} &= \frac{1}{x_i^{(n)}} \cdot \delta_{ij} \quad x_i^{(n)} > 0, \\ M_{ij}^{(n)} &= M_{\max} \cdot \delta_{ij} \quad x_i^{(n)} < 0, \end{aligned} \tag{10}$$

with $M_{\max}$ is an upper bound to prevent divergence.

The regularization parameter α is determined by enforcing statistical consistency of the fit, typically by minimizing $|\chi^2 - 1|$.

2.3.3. Statistical Model Consideration

For Gaussian noise, the goodness of fit is quantified using the reduced chi-squared statistic

$$\chi^2 = \frac{1}{N_c} \sum_i \left(\frac{f_i - (\mathbf{T}\boldsymbol{x})_i}{\sigma_i} \right)^2. \tag{11}$$

However, HXR measurements are governed by Poisson counting statistics. The inversion problem can therefore be formulated as a penalized log-likelihood maximization,

$$\ell = \sum_i [\mathbf{T}\boldsymbol{x}]_i - f_i \log [\mathbf{T}\boldsymbol{x}]_i \tag{12}$$

2.3.4. Maximum Likelihood – Expectation Maximization

Another approach following Poisson statistic is the Maximum Likelihood–Expectation Maximization (ML-EM) algorithm, also known as Richardson–Lucy iterative method [11]. The iterative update step is given by

$$x_k^{i+1} = x_k^i \sum_l T_{l,k} \frac{f_l}{\sum_m T_{l,m} x_m^i}. \tag{13}$$

After every step a non-negativity is enforced by setting the negative elements to be zero and to improve stability every n-th step smoothing operation can be performed by applying rolling average on x.

2.3.5. Tikhonov regularization for Poisson statistics

Tikhonov regularization can be modified by replacing χ^2 statistics with Poisson-log likelihood. This substitution should describe HXR measurements more precisely [12].

The solution of inversion problem is then formulated as maximization of log-likelihood

$$\ell = \sum_i \Big([\mathbf{T}\boldsymbol{x}]_i + \beta \Big) - \sum_i \Big(f_i \log([\mathbf{T}\boldsymbol{x}]_i + \beta) \Big) \tag{14}$$

2.4. Diagnostics of HXRs

In order to apply the reconstruction methods described above, reliable measurements of bremsstrahlung radiation are required. The following section therefore introduces the HXR diagnostic used in tokamak experiments and the detectors employed in this work.

2.4.1. Scintillation Detectors

Hard X-rays emission generated by runaway electrons are usually measured using scintillation-based spectrometers. The detection chain consists of a scintillator crystal converting incident photons into visible light, coupled to a photosensor that amplifies the optical signal [13]. Recently, the traditional photomultiplier tubes used as photosensors in scintillation detector assemblies are being supplemented by silicon photomultipliers.

Inorganic scintillators such as NaI(Tl) [14, 15], $CeBr_3$(Ce) [15], or $LaBr_3$(Ce) [16, 17] are commonly used for HXR detection due to their high light yield and good stopping power for photons in the keV–MeV range. Key material parameters affecting detector performance are light yield, decay time, and effective atomic number. High-Z materials provide better photoabsorption efficiency for hard X-rays, while short decay times improve count-rate capability.

The energy resolution of the detector is determined primarily by photon statistics and light collection efficiency.

2.4.1.1. Photomultiplier Tubes

Photomultiplier tubes (PMTs) are vacuum-based photon detectors. PMTs consists of an evacuated glass envelope containing a photocathode, a dynode chain, and a collecting anode. They provide high gain (10^6–10^7), low dark noise, and large active areas. However, PMTs require high bias voltages (1–2 kV). PMTs remain advantageous for low-noise applications and large-area detection, but their sensitivity to magnetic fields limits their use in compact tokamak environments [13].

2.4.1.2. Silicon Photomultipliers (SiPMs)

Silicon photomultipliers (SiPMs) are solid-state photon detectors consisting of arrays of Geiger-mode avalanche photodiodes operated above breakdown voltage. Each micro-cell acts as a binary photon counter, and the summed output signal is proportional to the number of triggered cells.

SiPMs offer PMT-like gain at much lower bias voltages (typically 25–70 V) and are immune to magnetic fields, making them well suited for tokamak applications. Their performance is governed by overvoltage, which controls gain and photon detection efficiency. However,

SiPMs exhibit temperature-dependent dark count rates and correlated noise (crosstalk and afterpulsing) [18].

The dynamic range and linearity is limited by the finite number of microcells.

2.5. Monte Carlo Modeling of Particle and Radiation transport

Monte Carlo (MC) methods simulate particle transport through matter using stochastic sampling of physical interaction processes. They are particularly suitable for modeling photon and electron interactions in complex geometries.

In this work, Geant4 [19] is used to model:

- bremsstrahlung photon production in plasma-facing components,
- photon transport through vessel structures,
- scintillator detector response, which *may* include
  - energy deposition,
  - *optical photon generation and transport*
  - *visible photon detection*

Geant4 provides modular electromagnetic physics models and detailed geometry handling, enabling realistic reproduction of the experimental setup.

Geometries in Geant4 can be constructed either programmatically within the implementation of `UserDetectorConstruction` class or imported from external descriptions. GDML (Geometry Description Markup Language) allow conversion of CAD models into Geant4-compatible geometry. For more complex CAD-based workflows, mesh-based approaches such as DAGMC [20] allows use of CAD geometries with Monte Carlo transport codes.

3. Experiments and Forward Modeling

The following chapter describes the experimental setup and forward modeling approach used in this work. First, the GOLEM tokamak and its diagnostic systems are introduced. This is followed by a description of the newly developed HXR detector assemblies and the Monte Carlo modeling used to simulate bremsstrahlung production, photon transport, and detector response.

3.1. Tokamak GOLEM

The GOLEM tokamak is a small circular-limiter tokamak operated at the Faculty of Nuclear Sciences and Physical Engineering (FNSPE) of the Czech Technical University (CTU) in Prague. It serves primarily as a platform for education, diagnostic development and basic plasma studies [21].

The device has a major radius $R_0 = 0.4\,\mathrm{m}$ and a limiter-defined plasma radius $a = 0.085\,\mathrm{m}$. The toroidal magnetic field reaches values up to $0.8\,\mathrm{T}$, while the plasma current is typically below $12\,\mathrm{kA}$. Discharge duration ranges $(10 - 45)\,\mathrm{ms}$. Other important GOLEM parameters can be found in Table 1.

Parameter	Value
Major radius R	$0.4\,\mathrm{m}$
Minor radius (vacuum vessel)	$0.1\,\mathrm{m}$
Plasma radius (limiter radius) a	$0.085\,\mathrm{m}$
Toroidal magnetic field B_t	$< 0.8\,\mathrm{T}$
Plasma current I_p	$< 12\,\mathrm{kA}$
Length of the discharge	$< 45\,\mathrm{ms}$
Central electron density $n_\mathrm{e}(0)$	$(0.5 - 3) \cdot 10^{19}\,\mathrm{m}^{-3}$
Central electron temperature $T_\mathrm{e}(0)$	$100 - 300\,\mathrm{eV}$

Table 1: Main parameters of the GOLEM tokamak [22].

The vacuum vessel consists of thin stainless-steel bellows surrounded by a 10 mm thick copper shell for passive stabilization. The working gas is typically hydrogen or helium. For educational purposes, the tokamak can be operated fully remotely via a web interface, allowing international students to design, execute, and analyze experiments [21].

Historically, GOLEM originates from the TM-1 *(tokamak malyj)* device constructed in the 1960s at the I. V. Kurchatov Institute in Moscow and later operated as CASTOR in the Institute of Plasma Physics before being relocated to CTU. Today, its main role is diagnostic development and reproducible small-scale plasma experiments [23].

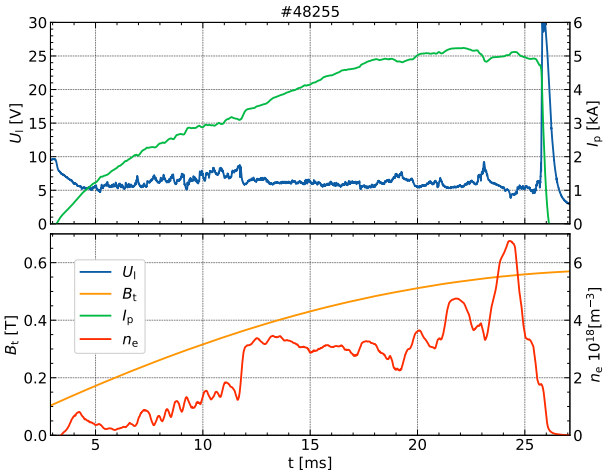

Figure 2: Basic plasma parameters of GOLEM tokamak discharge: Time evolution of loop voltage U_l, plasma current I_p, toroidal magnetic field B_t and electron density n_e.

3.1.1. Plasma Control systems

The plasma current and toroidal electric field are driven by a capacitor-bank-powered system. The discharge waveform is determined by the charging voltage and timing of thyristor switching, resulting in an RLC-type current evolution with limited active control.

Plasma position stabilization is implemented using a feed-forward control scheme. Since the windings are located outside the copper shell, magnetic field penetration is delayed by eddy currents, with a characteristic time constant of approximately 1 ms [24].

Recently, additional transformer windings were installed, allowing limited adjustment of the plasma current during discharge.

3.1.2. Diagnostic of GOLEM tokamak

Basic discharge parameters such as plasma current I_p, loop voltage U_l, toroidal magnetic field B_t are measured using standard magnetic diagnostics.

Plasma position is inferred primarily from four Mirnov coils located near the limiter. An additional set of 16 Mirnov coils in MHD ring are also available but not yet used for equilibrium reconstruction. Due to the conductive vacuum vessel and copper shell, eddy-current contributions must be removed. This is currently performed using reference “vacuum discharges”.

Optical diagnostics include two fast cameras used for qualitative estimation of plasma position and emission. Also, several spectrometers are available.

Line-integrated electron density is measured by a single-channel interferometer.

Hard X-ray emission is detected using multiple scintillation-based probes characterized in Table 2. These detectors are used to measure bremsstrahlung radiation associated with runaway electron losses on the limiter.

In addition, a Timepix3 pixel detector [25] may be used and an in-vessel runaway electron probe (DDRE) [26, 27] are under development for future measurements.

Scintillator	Yield [photons/MeV]	Decay time [ns]	Size	Photosensor
NaI(Tl)	38	230	$2'' \times 2''$	ET Enterprises 9266B
YaP(Ce)	18	27	$1'' \times 1''$	Hamamatsu R6094
$CeBr_3$(Ce)	60	19	$1'' \times 1''$	Hamamatsu R3998-02; Hamamatsu R1234A
LYSO(Ce)	30	45	$3 \times 3 \times 10$ mm	Broadcom AFBR-S4KTIA3315B
GaGG(Ce)	50	90	$3 \times 3 \times 10$ mm	Ketek PE3315-WB-TIA

Table 2: Parameters of scintillation detectors availabile on GOLEM [15, 28, 29]

3.2. New HXR Detector Assemblies

To extend the HXR diagnostic, three additional scintillation detectors based on LYSO(Ce) crystals were assembled and characterized.

Each detector is based on a LYSO crystal with dimensions $3 \times 3 \times 10$ mm. Crystals were wrapped in PTFE tape to improve light yield and optically coupled to a Broadcom AFBR-S4KTIA3315B SiPM modules.

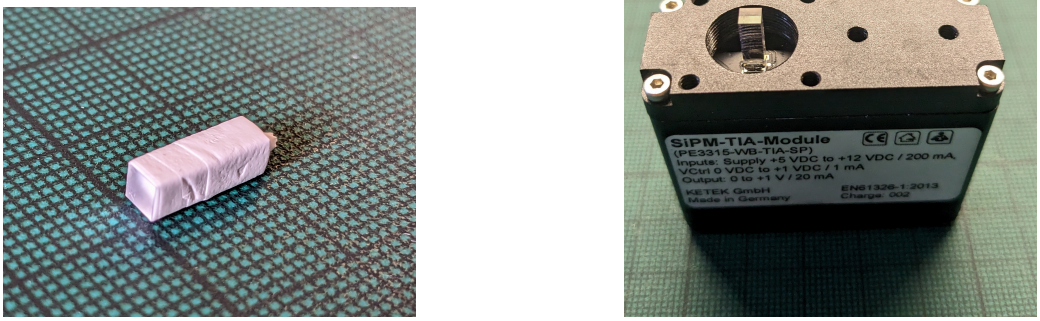

(a) LYSO crystal wrapped in PTFE tape (b) Broadcom SiPM module

Figure 3: LYSO:Ce detector assembly

Energy calibration and characterization were carried out using standard radioactive sources ^{137}Cs and ^{60}Co.

At present, a total of five similar LYSO-based detector assemblies are available for HXR diagnostic system. Two of these detectors employ Ketek PE3315-WB-TIA-TP SiPM modules, which the predecessor to the Broadcom AFBR-S4KTIA3315B module.

Calibration curves for LYSO detectors are shown in Figure 4.

Parameter	Value
Active Area	$3.0 \times 3.0\,\mathrm{mm}^2$
Microcell size	15 µm
No. of Microcells	38800
Recovery time	15 ns
Photo detection Efficiency	31 % (@ 410 nm)
Dark Count Rate	125 kHz/mm^3
Crosstalk Probability	18 %
Afterpulsing Probability	5 %

Table 3: Main properties of SiPM module [30]

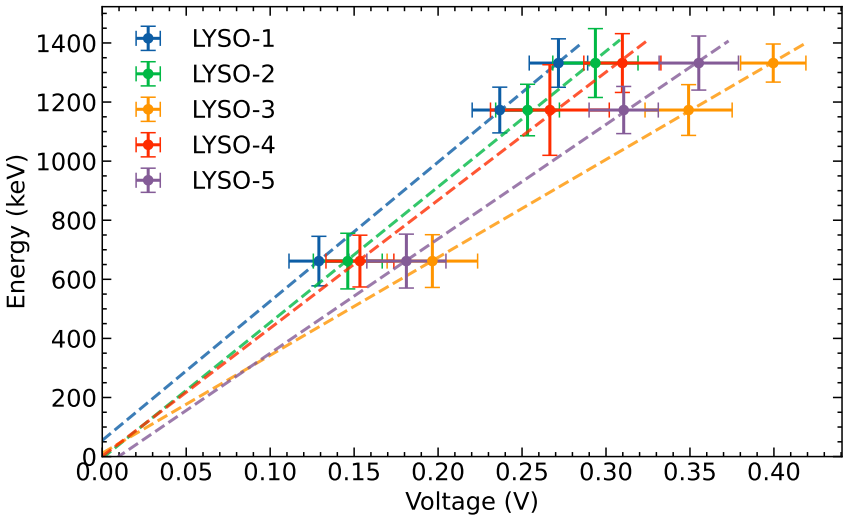

Figure 4: LYSO detectors calibration curves

3.3. Forward Modeling

The reconstruction of REs from measured HXR spectra requires a forward model linking the runaway electron distribution to the detector signal.

In the present stage of the project, the modeling effort has been developed progressively:

1. A detailed Monte Carlo model of the detector response,
2. A simplified study of runaway electron impact on limiter tiles in a magnetic field,
3. An integrated Geant4 model of bremsstrahlung generation and photon transport in the GOLEM geometry.

Currently the RE interaction and HXR transport are implemented within a single Monte Carlo simulation, future work will separate bremsstrahlung generation and photon transport into modular components to enable more efficient simulation runs.

All simulations were performed using the Geant4, version 11.1.3. The physics list *FTFP_BERT* was selected to describe standard electromagnetic processes to model photon–matter interactions over the energy range of interest.

3.3.1. Detector Response Modeling

Monte Carlo simulations were performed to model the detector response functions. These simulations provide the forward model required for the inversion of the measured HXR spectra.

The detector response function describes the probability distribution of measured pulse heights resulting from mono-energetic incident HXR photons. For LYSO-based $CeBr_3$-based detectors present on GOLEM response functions models response functions were generated by simulating mono-energetic photon sources.

3.3.1.1. Detailed LYSO detector model

For the LYSO detectors, a detailed geometrical and physical model was implemented. In addition to the scintillation crystal itself, the model includes Teflon wrapping for better optical performance, optical coupling between the crystal and the photosensor, and a simplified representation of the SiPM.

In this case the physics model also includes the Geant4 Optical Physics processes, which are treated separately from standard electromagnetic interactions. This enables explicit modelling of the full detection chain: conversion of incident HXR photons into scintillation light, generation of optical photons, their transport within the crystal volume, reflections at material boundaries, and their detection in the SiPM with respect to its quantum efficiency (QE).

This approach allows for a realistic estimation of the number of optical photons corresponding to a given deposited HXR energy. This can be used to estimate SiPM characteristics like afterpulsing, optical crosstalk, and potential nonlinearity effects at high photon counts.

(a) All optical photons. (b) Optical photons detected by SiPM.

Figure 5: Geant4 simulation of optical photons transport in LYSO crystal.

Tracking optical photons in Geant4 is computationally costly. As can be seen in Figure 5, most of the optical photons are not detected by SiPM. Moreover exact modelling of optical photon transport is limited by uncertainties in surface properties, reflectivity, and optical coupling parameters, which are often not precisely known.

From these simulations one can get the estimate of the number of photons which will be detected by SiPM and the spread in time. Figure 6 shows that the number of optical photons would not exceed the 10% of available microcells, so there is no non-linearity expected in HXR detection.

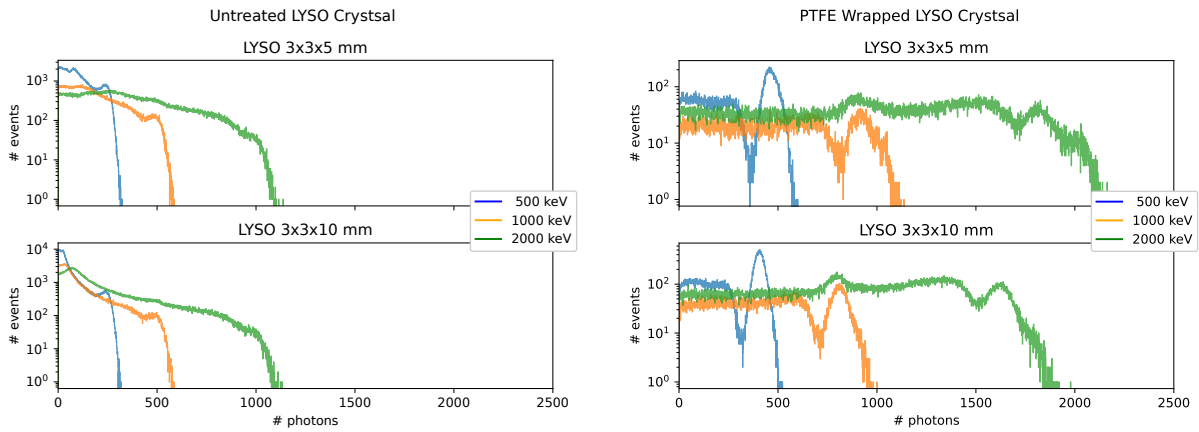

(a) Untreated LYSO crystal (b) LYSO crystal wrapped with PTFE tape

Figure 6: Geant4 simulation LYSO based detector with full optical cascade.

3.3.1.2. Simplified $CeBr_3$ detector model

Since classical PMTs do not need treatment for statistical nonlinearities like afterpulses and crosstalk simplified model was created.

Only the scintillation crystal and its mechanical housing were included in the Geant4 geometry, and optical photon transport was omitted. Instead, the total energy deposited in the scintillator by the incident HXR photons was recorded.

The detector response was then constructed by convolving the deposited-energy spectra with a Gaussian response function representing the intrinsic energy resolution of the detector system. The width of this Gaussian was determined from a combination of experimental calibration measurements and semi-analytical models of scintillator energy resolution.

3.3.1.3. Validation

The Geant4 detector model of LYSO was validated by comparing simulated spectra with experimental calibration measurements of ^{137}Cs

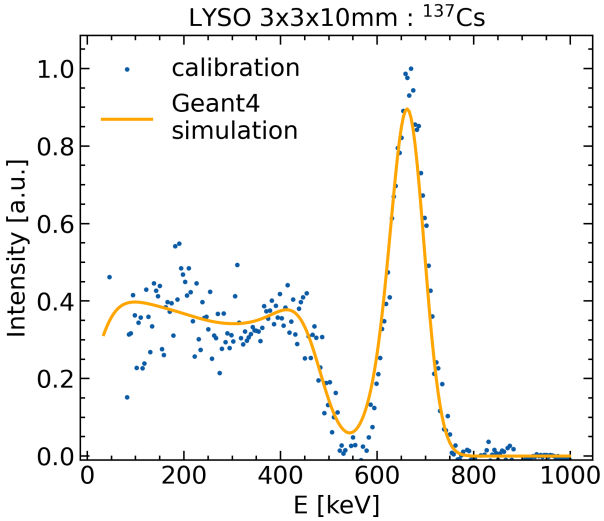

Figure 7: LYSO response to ^{137}Cs and Geant4 model

3.3.2. Simplified model of limiter tile in magnetic field

In a tokamak environment, the presence of a strong magnetic field dictates electron dynamics and the transport of secondary particles, which alters resulting bremsstrahlung.

There is fundamental difference between poloidal limiter which is on GOLEM tokamak and optimized toroidal limiters and PFC on modern tokamaks which have a small angle between magnetic field line and material surface.

In the case of poloidal limiter such as that used on GOLEM, the magnetic field lines intersect the limiter surface at comparatively large angles. As a consequence, the distribution of runaway electron impact angles is different as will be shown in Section 3.3.2.1. Also secondary electrons generated during the initial runaway–material interaction may be transported along magnetic field lines away from the original impact location and deposit their energy on distant plasma-facing components.

3.3.2.1. Magnetic angle and RE impact angle

The angle at which a runaway electron impacts a material surface is determined by the intersection of its helical trajectory with the local surface normal. In the presence of a uniform magnetic field, the runaway electron follows a helix defined by its parallel $v_{\parallel}$ and perpendicular velocity $v_{\perp}$ components with respect to the magnetic field direction.

The pitch angle θ can be defined as

$$\theta = \arctan\left(v_{\parallel}/v_{\perp}\right), \tag{15}$$

In the context of this work, pitch angles are considered over the range $\theta \in \langle 0, \frac{\pi}{2} \rangle$, corresponding to electron pitch $\left(v_{\parallel}/v_{\perp}\right) \in \langle 0, \infty)$

The impact angle β between the runaway electron trajectory and the material surface depends not only on the pitch angle but also on the relative orientation of the magnetic field on the initial phase of the gyromotion at the moment of impact. The impact angle cannot be expressed analytically and must be determined numerically.

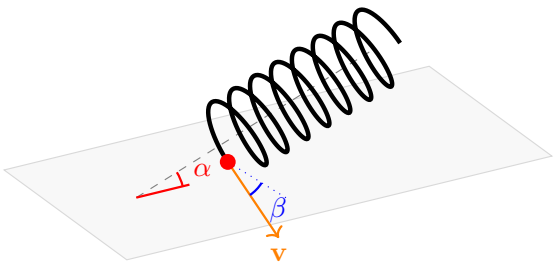

Figure 8: RE impact angle β and angle between material surface and magnetic field α.

For a given pitch angles θ was computed by sampling random initial phases of the helical trajectory. The distributions for selected magnetic field orientations and pitches in range $0 - 1.2$ are shown in Figures 9, 10.

For large aspect tokamak such as GOLEM the safety factor q can be expressed as

$$q \approx \frac{r}{R}\frac{B_\phi}{B_\theta} = \frac{r}{R}\frac{1}{\tan\alpha}, \tag{16}$$

For typical discharge parameters the q value lies in the range $3 - 12$ which corresponds to tilt of magnetic lines α in range $1° - 4°$.

In the case of toroidal limiter, the impact angles share considerable overlap, which is reduced for large angles, smaller q values.

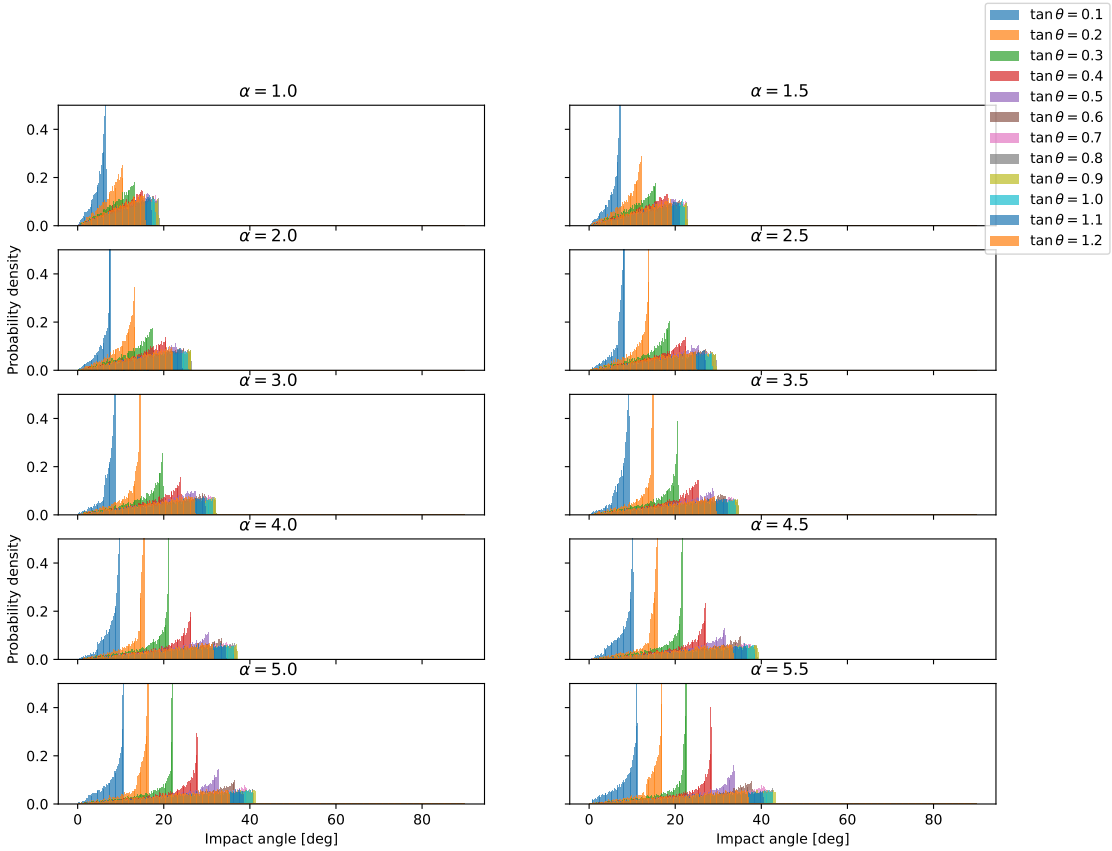

Figure 9: RE impact angles for toroidal limiter

For poloidal limiter (head-on collision between limiter plate and RE) the incidence angle follows the initial pitch, only for lower q the incidence angles starts to overap more.

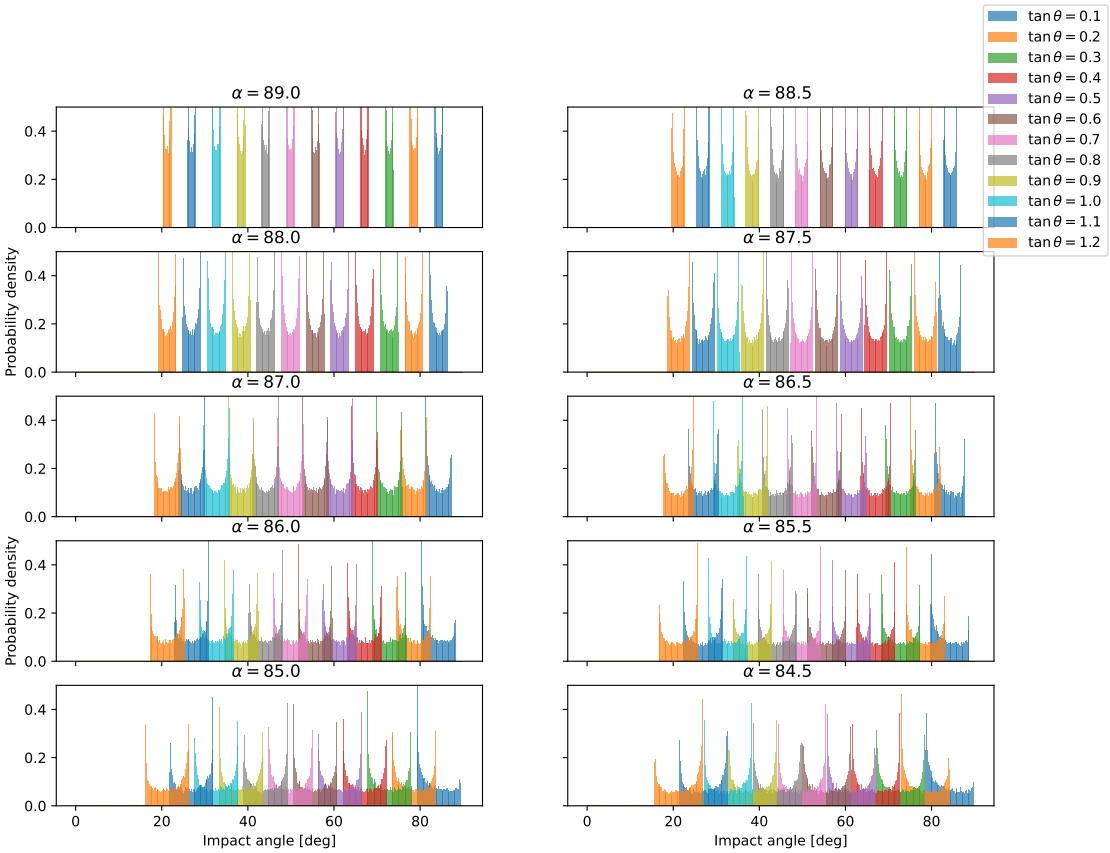

Figure 10: RE impact angles for poloidal limiter

3.3.2.2. Bremsstrahlung distribution

Because the pitch of RE affects the incidence angle, the distribution of bremsstrahlung radiation partly reflects the original RE pitch. For the case of poloidal limiter, this effect is more pronounced as can be seen in the Figure 11.

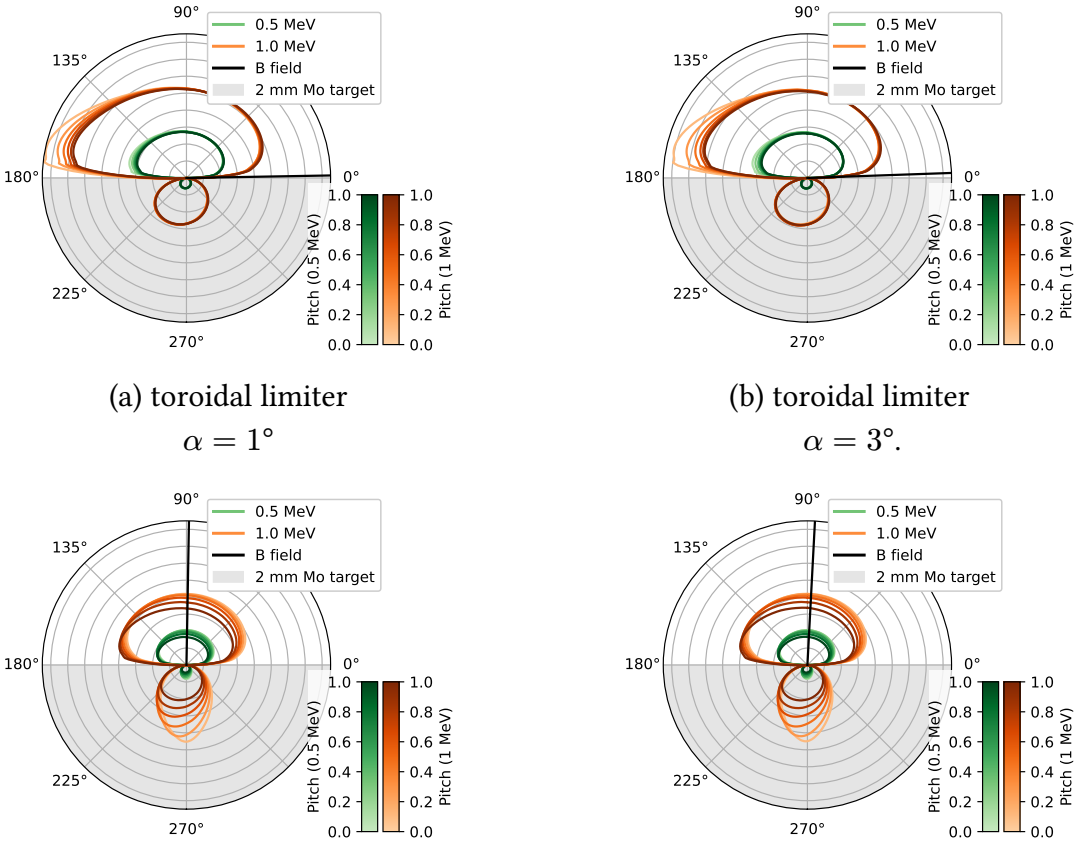

(a) toroidal limiter $\alpha = 1°$

(b) toroidal limiter $\alpha = 3°$.

(c) poloidal limiter $\alpha = 1°$

(d) poloidal limiter $\alpha = 3°$

Figure 11: Distribution of bremsstrahlung radiation from RE hitting the limiter tile. Two different limiter configurations and two magnetic angles α.

3.3.3. GOLEM Bremsstrahlung Model

A realistic Monte Carlo model of runaway electron interaction with the GOLEM poloidal limiter was implemented.

In the current implementation, bremsstrahlung generation, photon transport through the vessel, and detector interaction are treated within a single Geant4 simulation. The model includes:

- relativistic electron transport in magnetic field,
- bremsstrahlung production in molybdenum,
- photon propagation through vacuum vessel structures,
- scoring of HXR radiation around tokamak vessel.

3.3.3.1. Geometry Implementation

Several 3D models of the GOLEM tokamak exist, primarily developed for visualization and educational purposes [31]. These models lack components essential for radiation transport simulations, most notably the copper shell.

A detailed CAD model created in 2021–2024 [32] was evaluated for conversion into Geant4 geometry using GDML-based workflows. However, the high complexity and inconsistencies

in dimensions made direct conversion impractical without substantial simplification and remodelling.

Consequently, the GOLEM geometry was reconstructed directly within the Geant4 `DetectorConstruction` class using available technical drawings and in-vessel measurements.

The most significant uncertainty concerned the exact orientation and alignment of the poloidal limiter plates. To resolve this, structured-light 3D scanning of the limiter region was performed. Despite limitations imposed by vacuum compatibility and restricted access, the scans provided information to reconstruct limiter alignment for implementation in the Geant4 model.

The final geometry includes the vacuum vessel, copper shell, limiter plates, toroidal field coils, diagnostic ports, and transformer core. Minor mechanical details were omitted as they do not significantly influence photon transport.

3.3.3.2. Forward Runaway Electron Impact Model

Runaway electrons were injected toward the poloidal limiter with prescribed kinetic energies and pitch angles. The strike-point location was sampled at 32 poloidal positions along the limiter circumference. For each position, 13 pitch-angle values were simulated in the range $v_\perp/v_\parallel = 0 - 1.2$. A typical magnetic field configuration in the vicinity of the limiter was assumed.

Bremsstrahlung photons generated within the limiter material were recorded on a cylindrical scoring surface at radius of approximately 1.2 m, corresponding to feasible detector positions. For each simulation, the full photon energy spectrum was stored, allowing for energy-resolved post-processing and the construction of transfer matrices with explicit dependence on energy, pitch angle, and impact position.

Backscattered runaway electrons were not tracked further once they escaped the limiter material. While backscattering can carry up to approximately 40 % of the initial electron energy at large pitch angles (Figure 12), its contribution can be relevant to the experiment. But proper tracking would require prior knowledge of precise magnetic configuration or the simulations of all possible plasma column positions. These conditions cannot be satisfied without reliable real-time control of plasma position. The second approach would lead to extremely large computer time.

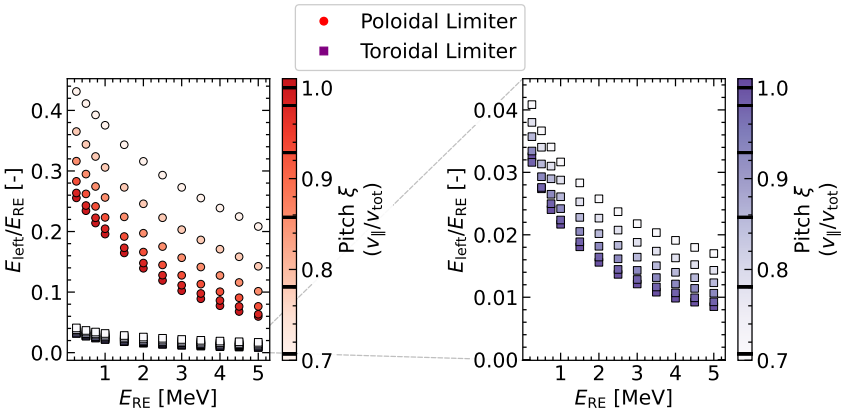

Figure 12: Fraction of backscattered REs for different energies, pitches and limiter orientations.

Therefore, it was decided to use collimators in experiments, so the bremsstrahlung radiation from backscattered electrons would be reduced.

For selected simulation run the full 3D distribution of photon flux was recorded. Two cases: low-field-side and high-field-side strike-points are shown in Figure 13.

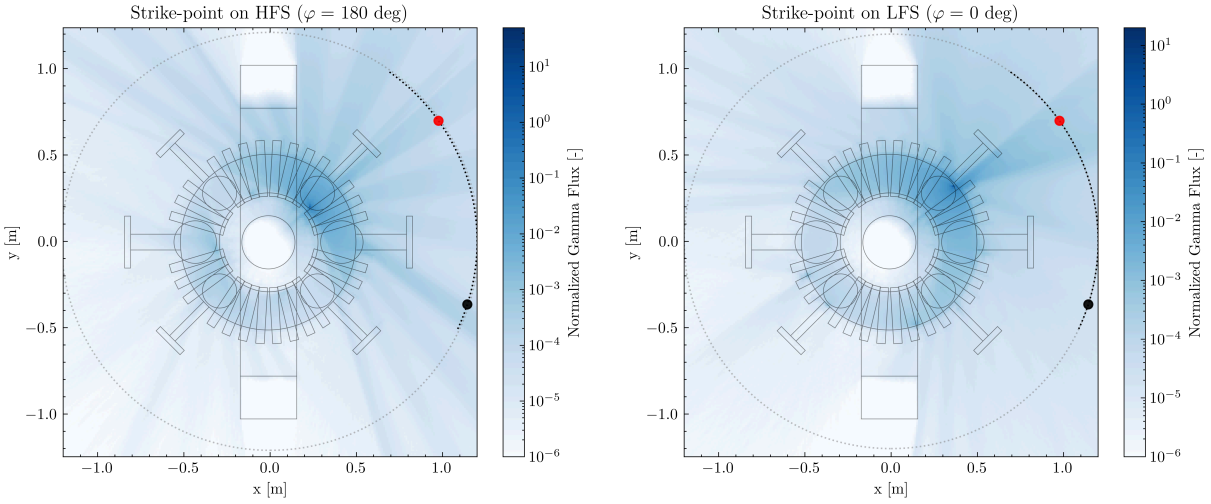

(a) HFS. (b) LFS.

Figure 13: Simulated photon flux distributions for RE strike-points on the high-field side (a) and low-field side (b). Top view, summed over the vertical z axis. Gray circle of diameter 1.2 m indicates Geant4 scoring surface. Points and highlighted part of scoring soring surface corresponds to x-axis span and detector locations on Figure 18.

3.3.4. Inversions

Once the forward model describing detector signals from RE parameters is developed, the inverse problem can be addressed. In this section, several inversion approaches are implemented and evaluated for reconstructing RE properties.

3.3.4.1. Energy Inversion

The runaway electron energy distribution can be inferred from the measured HXR spectrum. In the linear formulation introduced in Section 2.3, the forward model is written as

$$\boldsymbol{f} = \mathbf{D} \cdot \mathbf{B} \cdot \boldsymbol{x}, \tag{17}$$

where $\mathbf{B}$ describes bremsstrahlung emission and $\mathbf{D}$ represents the detector response matrix.

The inversion was performed using Tikhonov regularization. An example for discharge #48265 is shown in Figure 14.

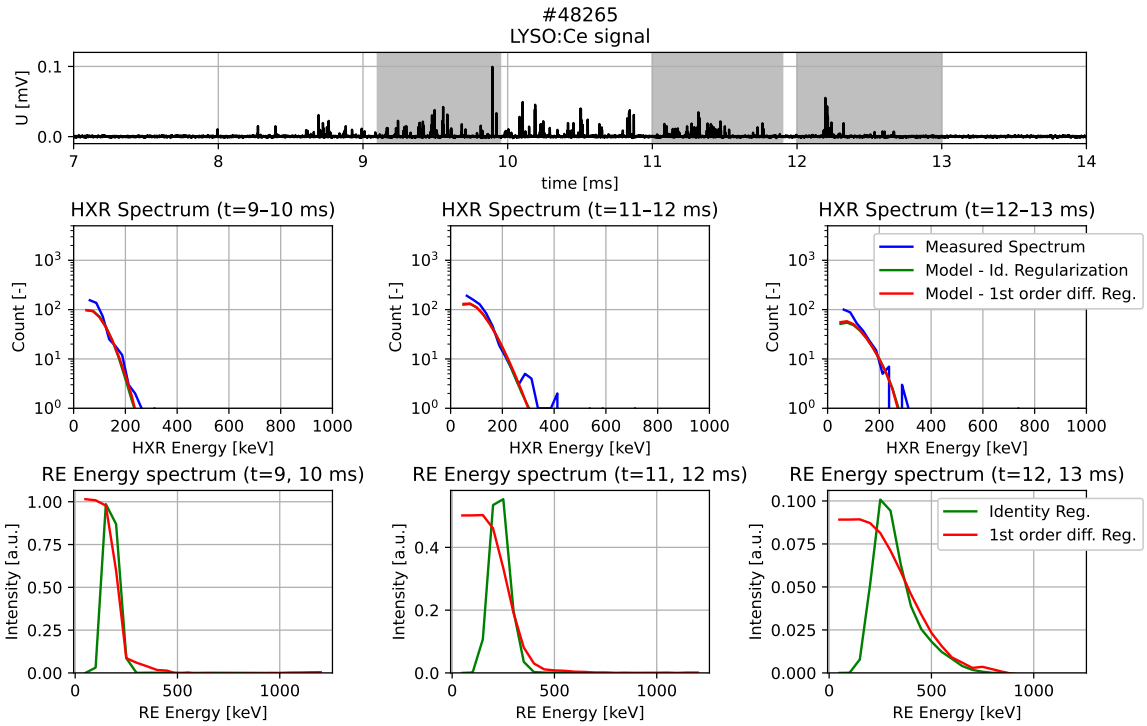

Figure 14: Results from RE inversion technique applied to recover RE energy distribution.
From the top: raw HXR data,
HXR spectrum in different parts of the discharge,
Results for the inversions.

The results demonstrate strong sensitivity to the regularization parameter. In particular, different low-energy tails of the reconstructed runaway spectrum can reproduce nearly identical HXR spectra.

Unfortunately, this inversion is sensitive to the quality of the data. Ideally without pile-up and with broad spectrum recorded. The pile-up can be limited with better shielding and collimation, but with trade-off to reduced count statistics statistic and some sensitivity loss for low HXR energies.

3.3.4.2. Position and Pitch Inversion

Bremsstrahlung emission is strongly anisotropic and therefore carries information about runaway pitch angle and strike-point location as is discussed in Section 3.3.2.2.

The inversion problem is formulated as

$$\boldsymbol{f} = \mathbf{T}\boldsymbol{x}, \tag{18}$$

where $\boldsymbol{x}$ represents the runaway source distribution defined on a discretized grid of:

- poloidal limiter positions,
- pitch-angle bins.

Each column of $\mathbf{T}$ corresponds to the detector response obtained from Monte Carlo simulations for a fixed strike-point and pitch.

In the present implementation, the inversion was restricted to fixed runaway energy due to limited simulation runtime.

3.3.4.3. Synthetic Validation and Algorithm Comparison

Before applying the inversion method to experimental data, its performance was assessed using synthetic data. In these benchmarks, known runaway source distributions were prescribed in the forward model, synthetic detector signals were generated, and the inversion algorithm was applied to recover the original parameters.

All single strike-point and pitch combinations were tested. Noise following the Poisson statistic corresponding to experimental conditions was included.

The following inversion methods were evaluated:

- Minimum Fisher Regularization (0th and 1st order),
- ML-EM (Richardson–Lucy),
- Non-negative least squares (NNLS),
- Maximum Poisson log-likelihood.

Scaling between number of used detectors and error for each method can be found on Figure 15.

For simplified single-location test cases, NNLS provided the lowest reconstruction error when a larger number of detectors was used. However, these benchmark conditions may not reflect realistic distributed runaway sources.

In practical experimental scenarios, MFR is preferable due to its ability to impose smoothness constraint.

On the other hand, Richardson–Lucy iterations do not pick up any information about pitch angle even though tests in [33] suggest this algorithm should be on par with Tikhonov regularization scheme.

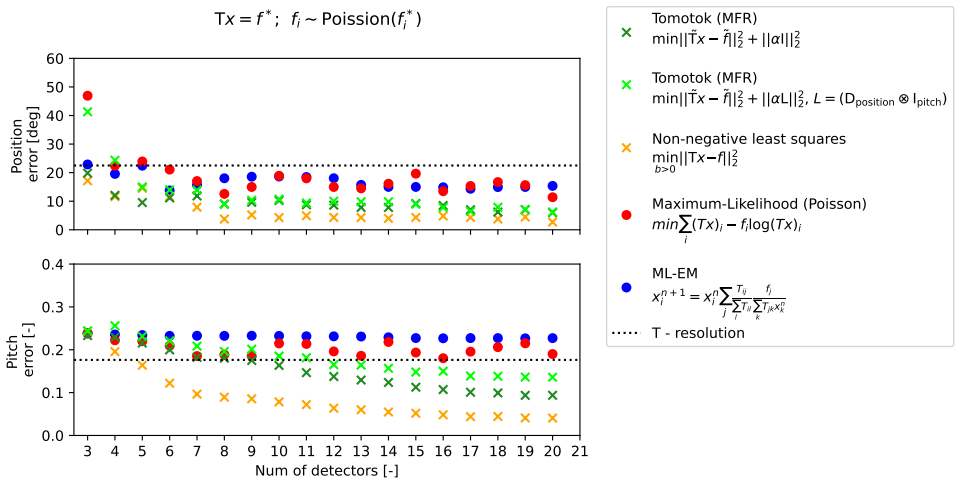

Figure 15: Dependence of inversion error on the number of detectors used for different inversion methods.

Since the error in pitch angle and RE position scales together (as can be seen on Figure 16), the accuracy in RE position reconstruction might be used as proxy for estimate of error in pitch angle.

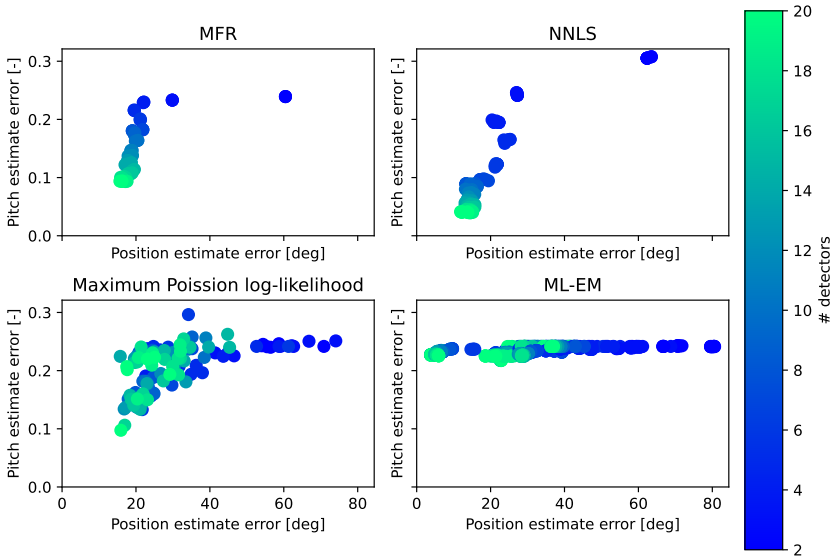

Figure 16: Scaling between error in RE position and pitch angle for different inversion schemes and number of detectors used.

Sensitivity to geometric misalignment was evaluated for 5, 10, and 20 detectors. The results (Figure 17) show that reconstruction accuracy degrades significantly with limited detector coverage.

These tests confirm that with the current experimental configuration, inversion results should be interpreted primarily as strike-point estimates, and inversion accuracy and robustness would benefit from larger detector coverage.

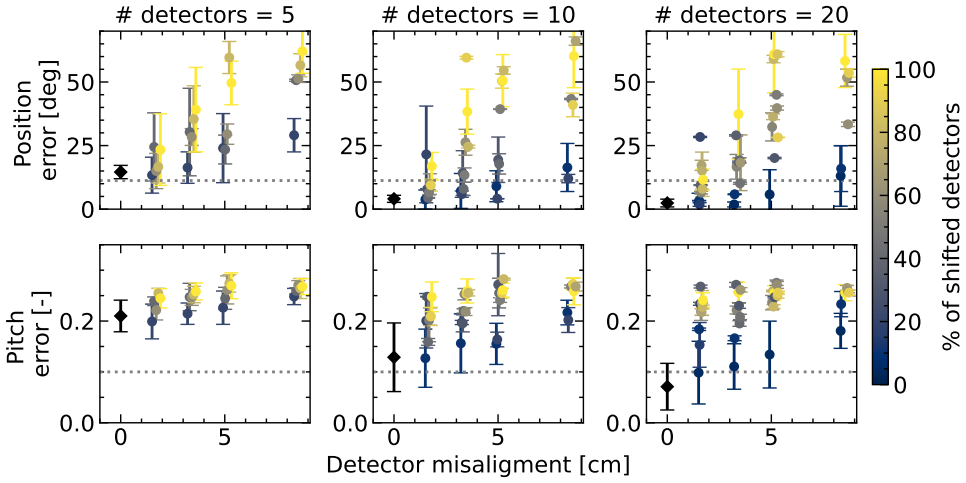

Figure 17: Effect of detector misalignment on inversion error

3.4. Experimental Application

After validating the inversions using synthetic data, the methods are applied to experimental measurements obtained on the GOLEM tokamak. The following section presents the analysis of these measurements.

3.4.1. Relative Strike-Point Shift Estimation

Before applying full tomographic inversion, a simpler method based on relative detector count-rate ratios was tested.

Due to the geometric asymmetry of GOLEM, the HXR linear combinations of flux ratios between selected detector pairs vary monotonically with poloidal strike-point location (poloidal angle φ) on the limiter.

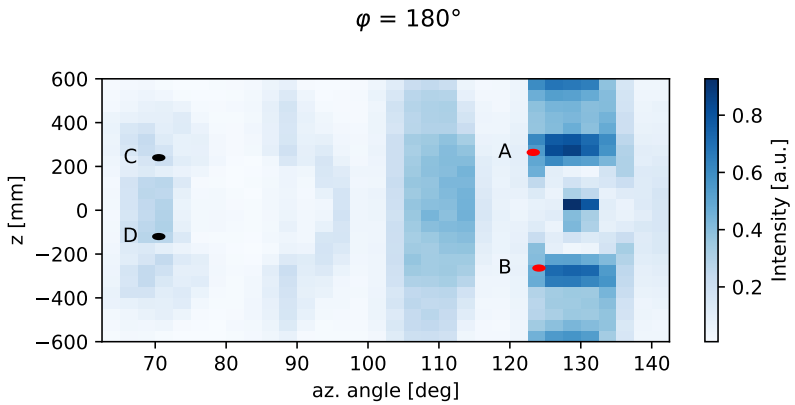

Figure 18: Distribution of HXR intensities near limiter for RE source on midplane HFS ($\varphi = 180°$), recorded by surface scorer in Geant4 simulation. Points A, B, C, D indicates detector placement.

For locations indicated as A, B, C, D on the are indicated on Figure 13 and Figure 18. Ratios between measured count-rates C_i

$$r_{\text{vertical}} = \frac{C_A}{C_B}, \tag{19}$$

$$r_{\text{radial}} = \frac{C_A + C_B}{C_C + C_D}, \tag{20}$$

were therefore used as proxies for vertical and radial shifts.

The behavior shown in Figure 19 enables qualitative tracking of runaway strike-point motion during discharge because it is monotonic for large ranges of RE loss position φ.

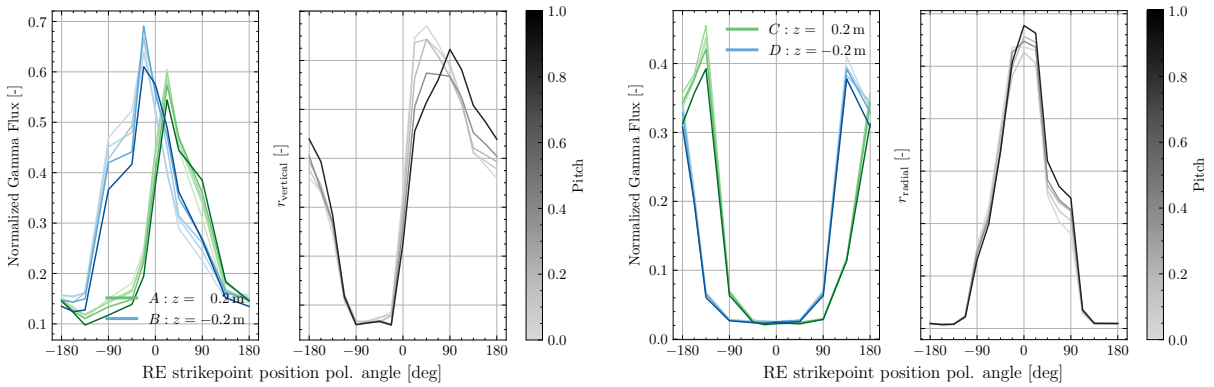

(a) $r_{\text{vertical}} = \frac{C_A}{C_B}$ (b) $r_{\text{radial}} = \frac{C_A+C_B}{C_C+C_D}$.

Figure 19: HXR flux with respect to RE position (pol. angle φ) and pitch (color-coded) for selected detector locations. Values r_{vertical} and r_{radial} allows to observe relative change of RE position.

A session dedicated to perturbation of plasma in GOLEM tokamak and measurement of RE strike-point position was performed for discharge #48255. The plasma position estimated from four limiter Mirnov coils and from fast cameras are shown in Figure 20, even though the cameras should be calibrated, the centroid or center of largest fitting circle does not fully agree with position from magnetic diagnostics. It is possible, the position of radial camera lines of sight has been calculated with systematic error of 40 mm. Even corrections in radial camera position, the calculated position of interaction point between plasma and limiter moves to opposite direction around 18 ms, this might be attributed to uncertainty in vertical position estimation.

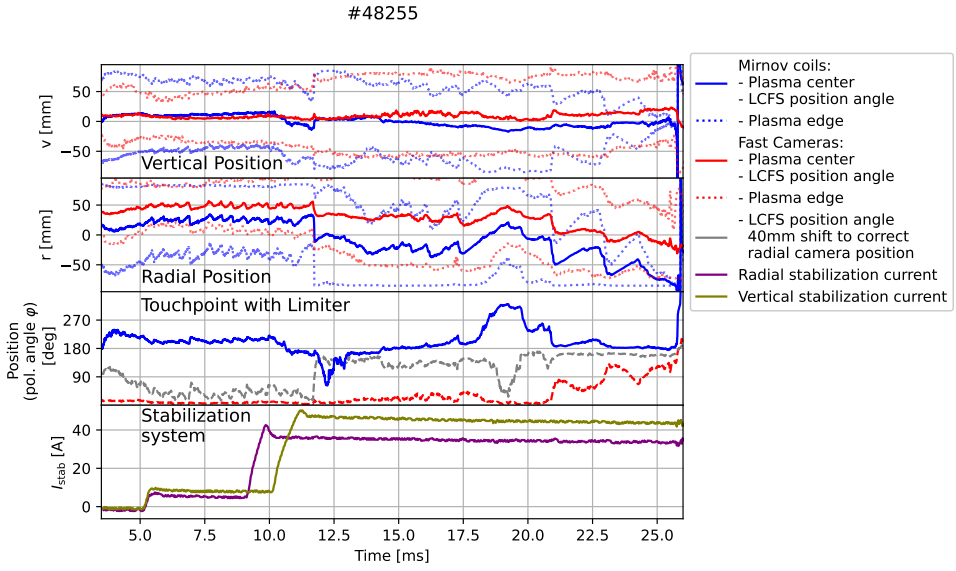

Figure 20: Estimates of plasma position from magnetic diagnostic and fast cameras for discharge #48255.

The time evolution of ratios of count-rate from HXR measurements are shown in figure Figure 21. The changes in plasma radial position are reflected in data from HXR probes.

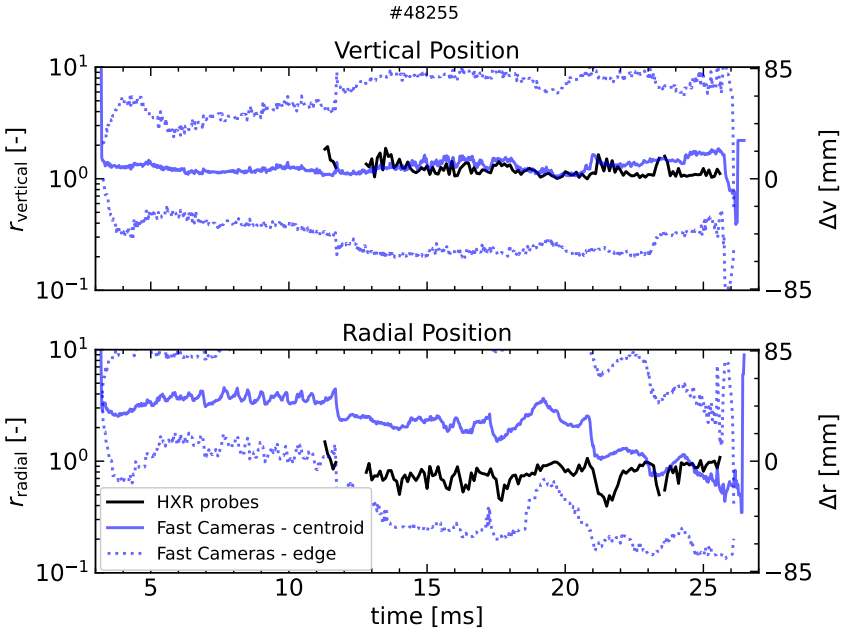

Figure 21: Comparison of plasma position and shifts of RE interaction position with limiter.

3.4.2. Results of strike-point and pitch inversion

For the discharges in previous the section, the tomographic inversion was conducted. Geant4 simulations were performed for 32 poloidal positions and multiple pitch-angle bins at energies of 0.5, 0.75, and 1 MeV.

Since the maximum RE energy is around 1 MeV the inversion was conducted for 1 MeV RE source (Figure 22).

The results in Section 3.3.4.3 suggest the current number of detectors available for inversion is too small to estimate RE pitch properly, we will be focused on RE strike-point estimate.

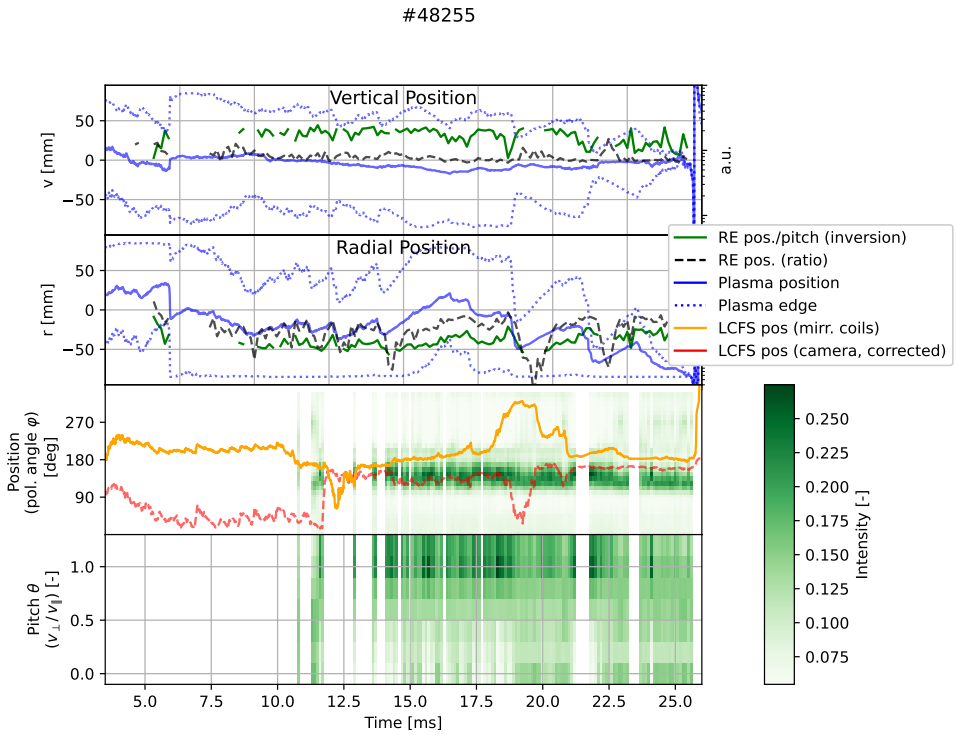

Figure 22: Full inversion on RE position and pitch for discharge #48255

The reconstructed mean strike-point location shows a qualitative agreement with magnetic diagnostics, although deviations are observed during periods of rapid plasma motion. These discrepancies may be related to radial plasma shifts not fully captured by the simplified inversion model or due to large error in plasma position estimates from magnetic diagnostic.

4. Conclusion and Future Work

This work establishes a forward-model-based framework for investigating RE losses in the GOLEM tokamak using bremsstrahlung HXR diagnostics. A Monte Carlo Geant4 model was developed to simulate RE impact on the poloidal limiter, photon transport in the vessel, and detector response. Inversion techniques were implemented and validated using synthetic data and applied to experimental discharges.

The results demonstrate that strike-point localization of runaway losses is feasible. However, reliable reconstruction of pitch-angle distributions is limited by detector number. The study therefore represents a proof-of-principle stage toward a more complete diagnostic method.

Several developments are planned:

First, the detector system will be improved. Dedicated collimators for the $CeBr_3$ and LYSO detectors will be designed to reduce pile-up and suppress background contributions. Design, mechanical integration, and calibration are expected to require approximately 1-2 months. In parallel, at least five additional SiPM-based LYSO detectors will be assembled to increase coverage and improve inversion stability. Assembly and characterization are estimated at 2–4 months.

Second, cross-validation with the newly installed DDRE [26, 27] probe will be performed. Correlating probe measurements with HXR inversion results will allow estimate of systematic uncertainties in strike-point reconstruction and pitch angle. This effort will require a dedicated experimental campaign and subsequent analysis, estimated at 4–6 months depending on status of the probe design maturity, DDRE probe data quality and forward model resolution.

Third, the current integrated Geant4 model will be modularized into two computational stages: (i) runaway electron impact and bremsstrahlung source generation, (ii) photon transport and detector response simulation. This separation will remove the need to repeatedly simulate electron transport in magnetic field during parametric scans, significantly reducing computational cost. And allowing to create forward model with larger density in RE parameter space. This will allow to perform full inversion on spectral data from multiple detectors, which would result in estimates of all RE parameters of interest - energy distribution, pitch-angle and location of RE loss. Implementation and validation of the modular framework are expected to require 4–6 months.

Further model refinement may include incorporation of bremsstrahlung in bulk plasma, either using Geant4, dedicated RE codes (GENESIS [34] or similar). This will allow evaluation of the relative importance of in-plasma emission compared to wall-generated radiation.

Finally, improvements in magnetic diagnostics are planned. Utilizing the full 16-coil Mirnov system and implementing state-space modeling for eddy-current compensation in the conductive vessel and copper shell will improve plasma position estimation. Development and validation is expected to require approximately 1 month.

With increased detector coverage and modular forward modeling, inversion methods evolve toward quantitative reconstruction of runaway phase-space dynamics.

Bibliography

[1] S. Ratynskaia *et al.*, "Runaway Electron-Induced Plasma Facing Component Damage in Tokamaks." Accessed: Sep. 07, 2025. [Online]. Available: http://arxiv.org/abs/2506.10411

[2] R. S. Granetz *et al.*, "An ITPA joint experiment to study runaway electron generation and suppressiona)," *Physics of Plasmas*, vol. 21, no. 7, p. 72506, 2014, doi: 10.1063/1.4886802.

[3] M. Vlainić *et al.*, "First Dedicated Observations of Runaway Electrons in the COMPASS Tokamak," *Nukleonika*, vol. 60, no. 2, pp. 249–255, Jun. 2015, doi: 10.1515/nuka-2015-0052.

[4] B. N. Breizman, P. Aleynikov, E. M. Hollmann, and M. Lehnen, "Physics of Runaway Electrons in Tokamaks," *Nuclear Fusion*, vol. 59, no. 8, p. 83001, Aug. 2019, doi: 10.1088/1741-4326/ab1822.

[5] H. Dreicer, "Electron and Ion Runaway in a Fully Ionized Gas. I," *Physical Review*, vol. 115, no. 2, pp. 238–249, Jul. 1959, doi: 10.1103/PhysRev.115.238.

[6] H. Dreicer, "Electron and Ion Runaway in a Fully Ionized Gas. II," *Physical Review*, vol. 117, no. 2, pp. 329–342, Jan. 1960, doi: 10.1103/PhysRev.117.329.

[7] J. Connor and R. Hastie, "Relativistic limitations on runaway electrons," *Nuclear Fusion*, vol. 15, no. 3, p. 415, Jun. 1975, doi: 10.1088/0029-5515/15/3/007.

[8] H. M. Smith, T. Fehér, T. Fülöp, K. Gál, and E. Verwichte, "Runaway electron generation in tokamak disruptions," *Plasma Physics and Controlled Fusion*, vol. 51, no. 12, p. 124008, Nov. 2009, doi: 10.1088/0741-3335/51/12/124008.

[9] J. Jackson, *Classical Electrodynamics*. Wiley, 1998.

[10] JET contributors *et al.*, "Current Research into Applications of Tomography for Fusion Diagnostics," *Journal of Fusion Energy*, vol. 38, no. 3–4, pp. 458–466, Aug. 2019, doi: 10.1007/s10894-018-0178-x.

[11] E. M. Khilkevitch, A. E. Shevelev, I. N. Chugunov, V. O. Naidenov, D. B. Gin, and D. N. Doinikov, "Application of Deconvolution Methods to Gamma-Radiation Spectra of Thermonuclear Plasma," *Technical Physics Letters*, vol. 39, no. 1, pp. 63–67, Jan. 2013, doi: 10.1134/S1063785013010161.

[12] J. M. Bardsley and N. Laobeul, "Tikhonov regularized Poisson likelihood estimation: theoretical justification and a computational method," *Inverse Problems in Science and Engineering*, vol. 16, no. 2, pp. 199–215, 2008, doi: 10.1080/17415970701404235.

[13] G. Knoll, *Radiation Detection and Measurement*. Wiley, 2010.

[14] V. Plyusnin, V. Kiptily, A. Shevelev, E. Khilkevitch, S. Gerasimov, and J. Mlynar, "Hard X-ray Bremsstrahlung of relativistic Runaway Electrons in JET," *Journal of Instrumentation*, vol. 14, no. 9, p. C9042, Sep. 2019, doi: 10.1088/1748-0221/14/09/C09042.

[15] J. Cerovsky *et al.*, "Progress in HXR Diagnostics at GOLEM and COMPASS Tokamaks," *Journal of Instrumentation*, vol. 17, no. 1, p. C1033, Jan. 2022, doi: 10.1088/1748-0221/17/01/C01033.

[16] L. Simons *et al.*, "A lanthanum bromide detector of runaway electrons for TCV," *Review of Scientific Instruments*, vol. 96, no. 9, p. 93501, 2025, doi: 10.1063/5.0277312.

[17] A. Shevelev *et al.*, "Study of runaway electron dynamics at the ASDEX Upgrade tokamak during impurity injection using fast hard x-ray spectrometry," *Nuclear Fusion*, vol. 61, no. 11, p. 116024, Sep. 2021, doi: 10.1088/1741-4326/ac2638.

[18] D. Renker and E. Lorenz, "Advances in solid state photon detectors," *Journal of Instrumentation*, vol. 4, no. 4, p. P4004, Apr. 2009, doi: 10.1088/1748-0221/4/04/P04004.

[19] J. Allison *et al.*, "Recent Developments in Geant4," *Nuclear Instruments and Methods in Physics Research Section A: Accelerators, Spectrometers, Detectors and Associated Equipment*, vol. 835, pp. 186–225, Nov. 2016, doi: 10.1016/j.nima.2016.06.125.

[20] P. Snouffer, R. Slaybaugh, and P. Wilson, "Criticality Benchmark Comparisons for DAGMC," *Transactions of the American Nuclear Society*, vol. 104, p. 440, 2011.

[21] V. Svoboda, B. Huang, J. Mlynář, G. Pokol, J. Stöckel, and G. Vondrášek, "Multi-Mode Remote Participation on the GOLEM Tokamak," *Fusion Engineering and Design*, vol. 86, no. 6–8, pp. 1310–1314, Oct. 2011, doi: 10.1016/j.fusengdes.2011.02.069.

[22] "Tokamak GOLEM wiki - front page." Accessed: Jan. 20, 2026. [Online]. Available: https://golem.fjfi.cvut.cz/wiki/

[23] "GOLEM Tokamak Wiki - History/index." Accessed: Jan. 20, 2026. [Online]. Available: https://golem.fjfi.cvut.cz/wiki/History/index

[24] "D. Kropackova (github) - PRPL Project - Summary & Outlook ." Accessed: Jan. 20, 2026. [Online]. Available: https://github.com/dakr11/PRPL/blob/39ce2dbc02d42da6c05082be63acc783d5d7ccb3/results_summary.md

[25] S. Malec *et al.*, "Timepix3 semiconductor pixel detector as runaway electron diagnostics at the GOLEM tokamak," Submitted to *Plasma Physics and Controlled Fusion*, 2026.

[26] S. Malec *et al.*, "Tokamak GOLEM for Fusion Education – Chapter 16: Bayesian Discharge Optimization, Artificial Neural Network Tomography, Runaway Electrons, Lithium Evaporator," in *Proceedings of the 51st EPS Conference on Controlled Fusion and Plasma Physics*, 2025.

[27] L. Lobko *et al.*, "In-vessel scintillation probe for direct detection of runaway electrons at the GOLEM tokamak," Submitted to *Plasma Physics and Controlled Fusion*, 2026.

[28] "CeBr3 - Cerium Bromide Scintillator Crystal." 2025. Accessed: Feb. 20, 2026. [Online]. Available: https://www.advatech-uk.co.uk/cebr3.html

[29] "LYSO Scintillation Material." 2025. Accessed: Jan. 10, 2026. [Online]. Available: https://luxiumsolutions.com/sites/default/files/2021-08/LYSO-Material-Data-Sheet.pdf

[30] "KETEK-PE33xx-WB-TIA-xP Datasheet." Accessed: Dec. 04, 2025. [Online]. Available: https://www.optoprim.it/wp-content/uploads/2020/05/KETEK-SiPM-Module-PE33xx-WB-TIA-xP.pdf

[31] “GOLEM Tokamak Wiki - Tools/VirtualModels/VirtualModel.” Accessed: Jan. 20, 2026. [Online]. Available: https://golem.fjfi.cvut.cz/wiki/Tools/VirtualModels/VirtualModel

[32] “GOLEM Tokamak Wiki - MH_CAD.” Accessed: Jan. 20, 2026. [Online]. Available: http://golem.fjfi.cvut.cz/wiki/Tools/MH_CAD/

[33] E. Panontin *et al.*, “Comparison of Unfolding Methods for the Inference of Runaway Electron Energy Distribution from γ-Ray Spectroscopic Measurements,” *Journal of Instrumentation*, vol. 16, no. 12, p. C12005, Dec. 2021, doi: 10.1088/1748-0221/16/12/C12005.

[34] M. Nocente *et al.*, “Conceptual design of the radial gamma ray spectrometers system for α particle and runaway electron measurements at ITER,” *Nuclear Fusion*, vol. 57, no. 7, p. 76016, May 2017, doi: 10.1088/1741-4326/aa6f7d.

Appendix

A. Publications

Article presenting results closely related to the work described in this document has been submitted for publication.

Title: Modelling and inversion of bremsstrahlung from runaway electrons on the GOLEM tokamak

Authors: M. Tunkl, L. Lobko, S. Malec, O. Ficker, J. Cerovsky, V. Svoboda, G. I. Pokol

Submitted to: Plasma Physics and Controlled Fusion: Special Issue on the 6th European Conference on Plasma Diagnostics (ECPD 2025)

Index of Figures

Index of Tables